




PAPER

Novel test field diversity method for demonstrating magnetic resonance imaging safety of active implantable medical devices

Aiping Yao^{1,2}, Earl Zastrow¹, Esra Neufeld¹, Maria Cabanes-Sempere³, Theodoros Samaras⁴ 
and Niels Kuster^{1,2}¹ Foundation of Research on Information Technologies in Society (IT²IS), 8004 Zurich, Switzerland² Department of Information Technology and Electrical Engineering, ETH Zurich, 8092 Zurich, Switzerland³ ZMT Zurich MedTech (ZMT) AG, 8004 Zurich, Switzerland⁴ Department of Physics, Aristotle University of Thessaloniki, 54124 Thessaloniki, GreeceE-mail: yao@itis.swiss**Keywords:** implant safety, radiofrequency fields, MRI, transfer function**Abstract**

Electromagnetic (EM) radiofrequency (RF) safety testing of elongated active implantable medical devices (AIMD) during magnetic resonance imaging (MRI) requires an RF response model of the implant to assess a wide range of exposure conditions. The model must be validated using a sufficiently large set of incident tangential electric field (\vec{E}_{tan}) conditions that provide diversified exposure. Until now, this procedure was very time consuming and often resulted in poorly defined \vec{E}_{tan} conditions. In this paper, we propose a test field diversity (TFD) validation method that provides more diverse exposure conditions of high fidelity, thereby decreasing the number of implant routings to be tested. The TFD method is based on the finding that the amplitude and phase of \vec{E}_{tan} along a single lead path in a cylindrical phantom can be sufficiently varied by changing the polarization of the incident 64 and 128 MHz magnetic fields inside standard birdcage test coils. The method is validated, its benefits are demonstrated, and an uncertainty budget is developed. First, the numerically determined field conditions were experimentally verified. The RF transfer function of a 90 cm long spinal cord stimulator was successfully validated with the TFD approach and excitation conditions that cover a > 10 dB dynamic range of RF-heating enhancement factors (for identical trajectory-averaged incident field strength). The new TFD method yields an improved and reliable validation of the AIMD RF response model with low uncertainty, i.e. < 1.5 dB, for both 1.5 and 3.0 T evaluations.

1. Introduction

To assess the risk of the radiofrequency (RF) electric (E) field induced in patients with an active implantable medical device (AIMD) during magnetic resonance imaging (MRI), a four-tier approach has been defined in ISO/TS 10974 (ISO 2018, Cabot *et al* 2013). The four tiers are designed such that the resulting overestimation of the local deposited power (or temperature rise) in tissue, due to the presense of an AIMD electrode, is decreased with increasing tier number. However, tiers with higher numbers require more and more complex and elaborate evaluations. For example, Tier 1 and Tier 2 represent the least complex test methods, but are based on the local maximum absolute exposure and produce the most conservative results. They are, therefore, suitable only for electrically short implants for which an overestimation of the risk is acceptable. The highest tier, Tier 4, requires the full simulation of all relevant clinical scenarios (including modeling of the patient, RF coils, and AIMD) and, accordingly, provides the most accurate estimation. Even today, Tier 4 is computationally expensive, as most commercial leads require μm discretization in a computational domain of several meters (i.e. days of simulation time for one clinical scenario using high performance computers). Therefore, this approach is practical for only very short (e.g. cochlea implants) or passive implants in limited clinical scenarios. On the other hand, pure *in vitro* investigation of AIMD with long leads (Calcagnini *et al* 2008, Mattei *et al* 2008, Nordbeck *et al* 2009, Mattei *et al* 2015) is cumbersome and does not

take into consideration the anatomical heterogeneity of the human body with its many organs and tissues. Therefore, the only practical tier for the evaluation of AIMD with elongated leads currently is Tier 3.

Tier 3 is designed to alleviate the computational burden of Tier 4 by splitting the evaluation into two steps. In the first step, the entire range of *in vivo* exposure conditions of the AIMD in patients is obtained *in silico*, i.e. by simulations. For typical implants, such as pacemakers or spinal cord stimulators, this includes millions of individual exposure conditions composed of combinations of RF coils that represent all installed geometries, polarizations of the magnetic field, varying patient anatomies in different postures and imaging positions, as well as clinical lead trajectories. These exposure conditions are evaluated as tangential E-fields ($\vec{E}_{\text{tan}}(l)$) along the implant length. In the second step, an AIMD RF transfer function model for each electrode of the AIMD (Park *et al* 2007) is created independently according to Tier 3 (ISO 2018). The transfer function describes, how (scaling amplitude and phase-shift) a very local tangential field exposure at a position along the AIMD contributes to the induced E-field in the tissue at critical locations of the implant (see section 2), such as electrodes. The combination of both the exposure condition \vec{E}_{tan} and the AIMD RF transfer function, together with knowledge about the local tissue properties, enables the determination of the local power deposition or local temperature increase. As the results directly depend on the quality of the AIMD RF transfer function, its conclusive and robust validation plays a key role for a reliable and accurate power deposition estimation.

To date, validation tests generally comprise a test phantom filled with tissue simulating medium (TSM) in which the AIMD is submerged. To achieve multiple distinct \vec{E}_{tan} characteristics, different combinations of phantoms and implant routings are commonly used during the validation process (ISO 2018, Zastrow *et al* 2011), the objective of which is to verify by measurements the predicted values of local deposited power, as estimated with the AIMD RF transfer function model. However, the number of achievable distinct sets of incident fields \vec{E}_{tan} is limited, due to the long AIMD length (> 50 cm) and the limited phantom size. Moreover, the separation distance from the phantom walls and between AIMD segments needs to be considered to minimize the influence from phantom boundary reflections and scattering at adjacent AIMD lead segments (Zastrow *et al* 2017). These considerations add constraints on the implant placement during the test procedure and reduce the achievable diversity of \vec{E}_{tan} (e.g. less than four distinct \vec{E}_{tan} are available for an AIMD with a lead length of 90 cm under circularly polarized exposure). In addition, testing time and characterization efforts increase with the number of test configurations for methods based on different combinations of phantoms and routings (more than one hour per test configuration). Furthermore, remounting of the implant during each test configuration introduces additional positioning uncertainties.

To achieve an improved scheme for the AIMD RF transfer function validation, a way of gaining \vec{E}_{tan} diversity through manipulation of the RF coil exposure instead of the implant geometry is proposed in this work. The proposed test field diversity (TFD) method is applied to long AIMDs (section 2) to establish a set of transfer function validation tests that benefit from high test condition diversity and fidelity along the AIMD. The TFD is derived directly from the idea of RF shimming (Brink *et al* 2015) used to control the E-field distribution inside a birdcage RF coil. The incident field distribution can also be manipulated using more sophisticated and difficult to implement techniques, like the employment of passive scatterers, such as passive resonant RF coils, that could be placed at various locations around the phantom, or dielectric shimming (de Heer *et al* 2012, Brink *et al* 2016).

2. Materials and methods

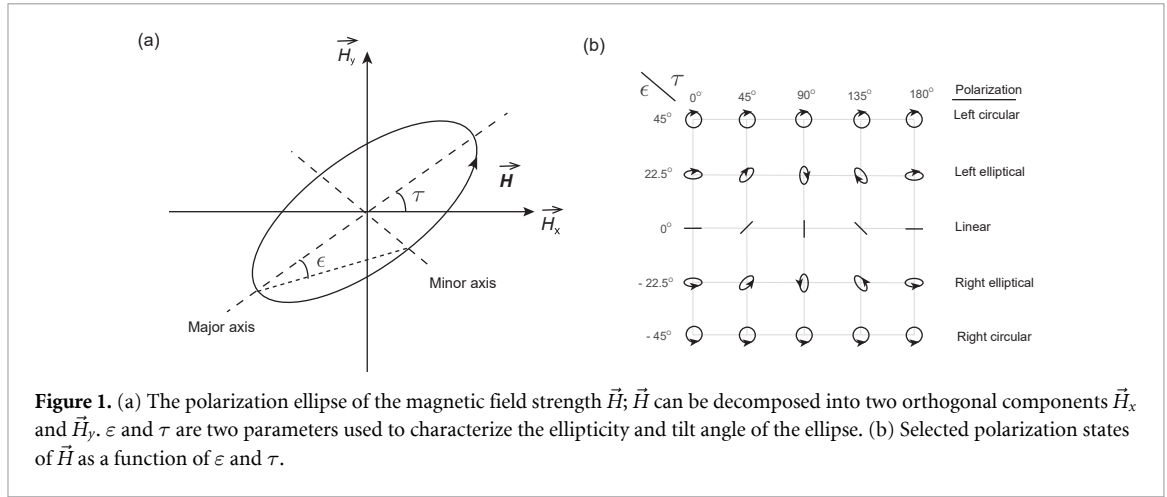
The TFD method is designed to validate an independently determined AIMD RF transfer function with a minimal physical set of routings inside a phantom filled with TSM, by changing the polarization of the incident field radiated from the MRI birdcage test system (i.e. diversifying the exposure \vec{E}_{tan}).

Parameters used to characterize field polarization ellipses are introduced in section 2.1. The incident condition definition is explained in section 2.2. A dedicated exposure setup for validation has been established and is described in section 2.3. Section 2.4 summarizes the application of the TFD method for the validation of an implant RF transfer function, with a 90 cm spinal cord stimulator lead as an example implant under test (IUT).

2.1. Polarization ellipse

The polarization state of any electromagnetic (EM) wave can be represented as a tilted ellipse with specific ellipticity (roundness) and tilt angle. Figure 1(a) illustrates a generic elliptically-polarized magnetic field strength (\vec{H}) with right-hand rotation; the two parameters ϵ and τ define the ellipticity and tilt angle of the field polarization (Kraus and Carver 1973). The ellipticity (ϵ) is defined as:

$$\epsilon = \alpha \cdot \arccot(\text{AR}) \quad (1)$$



where AR is the axial ratio of the polarization ellipse, defined as the ratio of the magnitude of the major axis of the polarization ellipse to that of the minor axis; α indicates the rotation of the polarization ellipse, $\alpha = 1$ for left-hand rotation, $\alpha = -1$ for right-hand rotation. For instance, for left-hand circularly polarized fields, $\epsilon = 45^\circ$; for right-hand polarized fields, $\epsilon = -45^\circ$; for linearly polarized fields, $\epsilon = 0^\circ$. Figure 1(b) illustrates the polarization states of EM fields in the (ϵ, τ) space.

2.2. Incident condition definition

Based on the superposition principle of the Maxwell equations, the combined magnetic field strength vector for birdcage RF coils with N individual channels can be expressed as:

$$\vec{H}_{\text{total}} = \sum_{i=1}^N \{v\}_i \vec{H}_i \quad (2)$$

where $\{v\}_i$ (i th element of v) are complex driving coefficients and \vec{H}_i are the magnetic field strength vectors of channel i , respectively. For RF coils with two orthogonal channels (channel x and channel y):

$$\vec{H}_{\text{total}} = \{v\}_x \vec{H}_x + \{v\}_y \vec{H}_y \quad (3)$$

For tangential E-field strengths along a certain implanted lead, $\vec{E}_{\text{tan},x}$ and $\vec{E}_{\text{tan},y}$ (for the x and y channels), the total tangential E-field strengths can be expressed as:

$$\vec{E}_{\text{tan},\text{total}} = \{v\}_x \vec{E}_{\text{tan},x} + \{v\}_y \vec{E}_{\text{tan},y} \quad (4)$$

However, to ensure that RF power deposition enhancement factors remain comparable (a requirement when selecting diversified \vec{E}_{tan} exposure conditions), the exposure magnitude is scaled such that $|\overline{\vec{E}_{\text{tan},\text{total}}}| = 1$, namely,

$$\vec{E}_{\text{tan},\text{total}} = (\{v\}_x \vec{E}_{\text{tan},x} + \{v\}_y \vec{E}_{\text{tan},y}) \left(|\{v\}_x \vec{E}_{\text{tan},x} + \{v\}_y \vec{E}_{\text{tan},y}| \right)^{-1} \quad (5)$$

where the overline denotes the value of a quantity averaged along the AIMD trajectory.

2.3. Exposure systems

Two exposure systems were used for the experimental assessment: (i) a 64 MHz birdcage (length = 65 cm, diameter = 70 cm) (MITS1.5, ZMT Zurich MedTech AG, Switzerland) with an iso-symmetrically loaded 44 cm-diameter cylindrical phantom filled with TSM ($\epsilon_r = 78$, $\sigma = 0.47 \text{ Sm}^{-1}$) to the height of 19 cm, and (ii) a 128 MHz birdcage (length = 50 cm, diameter = 70 cm) (MITS3.0, ZMT Zurich MedTech AG, Switzerland) loaded with the same phantom. The Q-I ports can be driven with RF square pulses with 40% duty cycle over a wide range of phase differences and amplitude ratios.

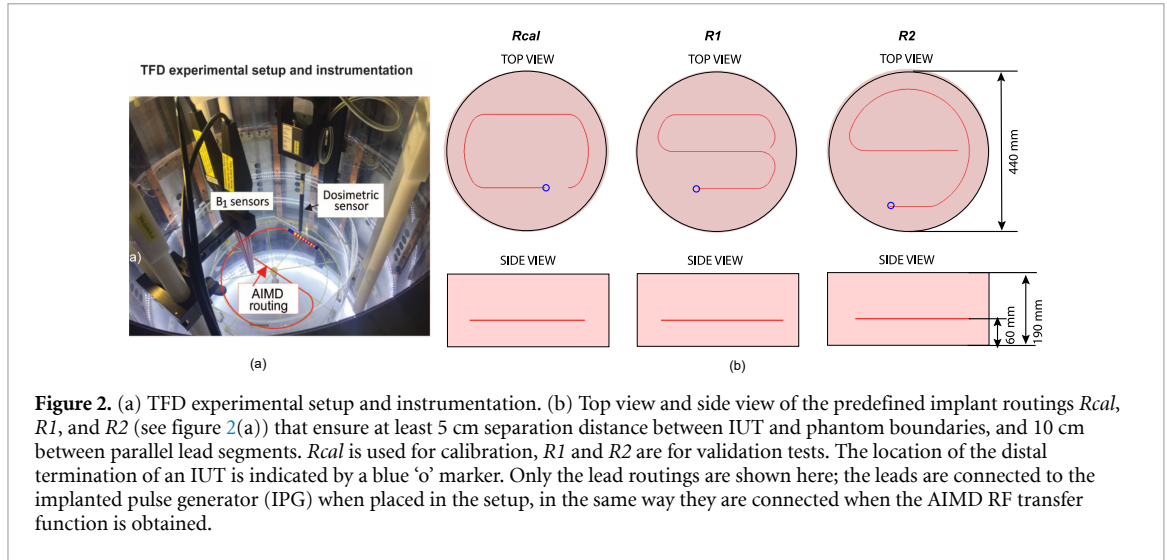


Figure 2. (a) TFD experimental setup and instrumentation. (b) Top view and side view of the predefined implant routings *Rcal*, *R1*, and *R2* (see figure 2(a)) that ensure at least 5 cm separation distance between IUT and phantom boundaries, and 10 cm between parallel lead segments. *Rcal* is used for calibration, *R1* and *R2* are for validation tests. The location of the distal termination of an IUT is indicated by a blue 'o' marker. Only the lead routings are shown here; the leads are connected to the implanted pulse generator (IPG) when placed in the setup, in the same way they are connected when the AIMD RF transfer function is obtained.

Three implant routings were established with the following design goals: (i) minimal reflections from truncated boundaries, (ii) minimal scattering between two parallel segments of the implant leads, and (iii) support for implant lengths up to 90 cm. This ensures at least 5 cm separation between the implant lead to any truncated boundaries and at least 10 cm separation between parallel segments of the implant as determined by Zastrow *et al* (2017). Different polarization states of the B_1 field are achieved by controlling the driving vectors of the two-port RF coils, which, are monitored by two optical magnetic field probes H1TDSx/MR (SPEAG, Zurich, Switzerland) with a frequency range of 10 MHz to 6 GHz and a dynamic range of 120 dB at 1 Hz resolution bandwidth. The accuracy in amplitude and phase is better than 0.4 dB and less than 3%, respectively. Figure 2 illustrates the test setup and the three implant routings used in this work. The first routing (*Rcal*) is used to calibrate the transfer function. Two other routings (*R1* and *R2*) are used for the purpose of validating the transfer function approach, the transfer functions themselves, as well as to demonstrate the TFD approach indeed provides sufficiently independent exposure conditions to constrain transfer function errors (see section 4).

To validate the exposure system, the RF-coils are driven to achieve three reachable polarization states: P1 (left circular polarization), P2 (linear polarization), and P3 (right circular polarization). The spatial distributions of the total E-field strength over the plane where the IUT will be located are experimentally verified by measuring the field strength components with the near-field pseudo-vector E-field probe EU2DV3 (SPEAG, Zurich, Switzerland) (Pokovic *et al* 2000) and compared with values obtained from full-wave simulations of the exposure setups with the Sim4Life software platform (ZMT Zurich MedTech AG, Switzerland). The unique probe design enables accurate determination of the polarization ellipse and the magnitude of the induced fields. The linearity of the probe is ± 0.2 dB with a dynamic range of 10 Vm^{-1} to 1000 Vm^{-1} and the sensor positioning uncertainty is less than 0.3 mm. The deviation between experimental and numerical evaluations of the total E-field strength was found to be less than the total (simulation and measurement) combined standard uncertainty of 0.2 dB ($k = 1$).

2.4. Tier 3 RF transfer function

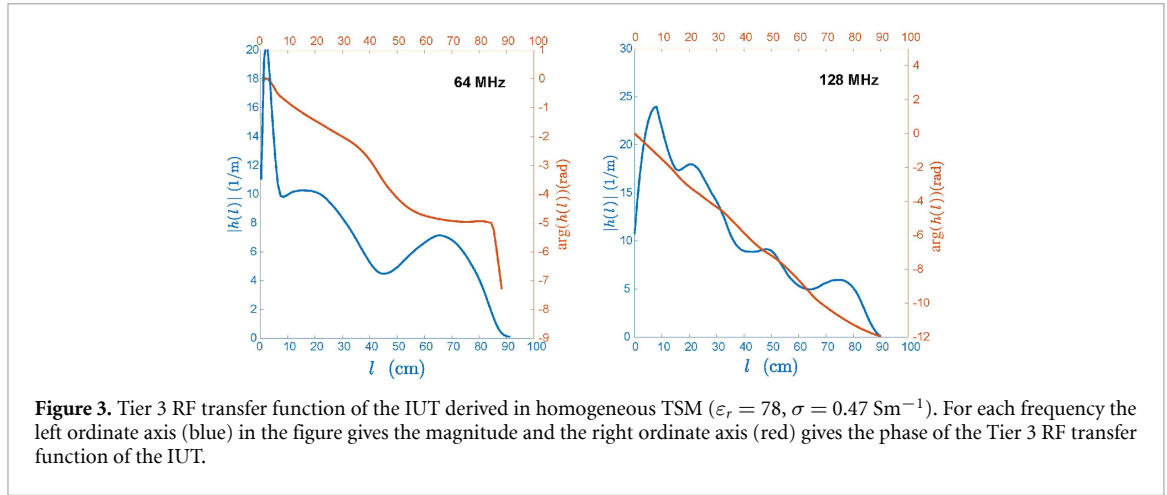
To characterize the implant-RF interactions, the transfer function concept is introduced in the Tier 3 approach of ISO/TS 10974 Clause 8 for the determination of the RF-induced heating (ISO 2018, Park *et al* 2007). Figure 3 illustrates the Tier 3 RF transfer functions of the IUT at 64 MHz and 128 MHz, respectively, derived in homogeneous TSM according to the piecewise excitation method described in Zastrow *et al* (2016). The principal assumption of the method is that the total induced field strength at an electrode is the superposition of the induced field contributions from local incident fields along the implant (Park *et al* 2007). Therefore, the method offers a sound strategy for the determination of the total RF-induced power deposition resulting at each electrode from any incident field condition.

For the Tier 3 (complex) RF transfer function $h(l)$ magnitude to be normalized such that

$$1 = \left(\int_0^L h(l) dl \right) \left(\int_0^L h(l) dl \right)^*, \quad (6)$$

the RF power deposition enhancement of the IUT is expressed as:

$$P_{\text{dep}} = \frac{P_0}{|E_0|^2} \left(\int_0^L h(l) \vec{E}_{\text{tan}}(l) \cdot d\hat{l} \right) \left(\int_0^L h(l) \vec{E}_{\text{tan}}(l) \cdot d\hat{l} \right)^*, \quad (7)$$



where P_{dep} is the power deposition of the IUT under the incident condition \vec{E}_{tan} defined in (4), $\hat{d}l$ is the tangential unit vector at location l along the IUT, $\vec{E}_{\text{tan}}(l)$ is the tangential electric field strength at location l along the IUT, and P_0 is the power deposition of the IUT under a unit iso-electric tangential incident field of complex magnitude $E_0 = 1e^{i\phi_0} \text{ Vm}^{-1}$ (ϕ_0 is a constant).

P_0 is calibrated by using routing R_{cal} in combination with ten excitation conditions. A dosimetric probe (EX3515, Zurich, SPEAG) is used for that purpose, and calibration has been separately performed at 64 MHz and 128 MHz.

2.5. RF power deposition derived from the AIMD transfer function

The RF power deposition enhancement factor of the IUT, χ , is defined as follows:

$$\chi = P_{\text{dep}}/P_0 \quad (8)$$

The theoretical RF power deposition enhancement factor (hereafter denoted as χ_{Tier3}), which is derived from the Tier 3 AIMD transfer function, can be expressed by combining (7) and (8) as:

$$\chi_{\text{Tier3}} = \frac{1}{|E_0|^2} \left(\int_0^L h(l) \vec{E}_{\text{tan}}(l) \cdot \hat{d}l \right) \left(\int_0^L h(l) \vec{E}_{\text{tan}}(l) \cdot \hat{d}l \right)^* \quad (9)$$

Two other quantities, χ_0 and χ_ϕ , are used throughout the rest of the paper, where χ_0 is the enhancement factor of the IUT under a unit iso-electric incident condition. By definition (normalization of $h(l)$), $\chi_0 = 1$. χ_ϕ is the maximum enhancement factor achievable with an \vec{E}_{tan} of complex magnitude of the form $1e^{i\phi(l)}$ (iso-magnitude exposure condition), where $\phi(l)$ is an arbitrary phase function. It can be achieved, e.g. by setting $\phi(l) = -\arg(h(l))$. In this case, $\chi_\phi = \left(\int_0^L |h(l)| dl \right)^2$.

For any unit iso-magnitude exposure condition, $0 \leq \chi_{\text{Tier3}} \leq \chi_\phi$. When the incident field does not have a constant magnitude (but still has the same length-averaged magnitude), phase functions can be found that result in values of χ_{Tier3} that exceed χ_ϕ . However, for real-world conditions, χ_ϕ is not far from being an upper bound (figure 4).

2.6. RF power deposition measured from TFD experiments

To maximize the validation power, exposure conditions were selected such that they sample a wide range of expected enhancement factors, with the assumption that large enhancement factor differences must be the result of important exposure differences (either because of important changes in the E_{tan} phase distribution, or because of a shift of high exposure locations to another region of the transfer function $h(l)$). While the selection of exposure conditions based on extensive sampling of the full range of achievable enhancement factors intuitively suggests that they are indeed sufficiently independent (orthogonal), it does not constitute a mathematical guarantee. Section 4 provides a systematic mathematical framework that could be used to further optimize the selection of exposure conditions and also demonstrates that the selected conditions are sufficient to impose tight limits on possible transfer function errors.

Twenty exposure conditions of the IUT were selected in this study (1–10 for routing $R1$, 11–20 for routing $R2$, see figure 2) based on the distribution of χ_{Tier3} (τ, ϵ) of the IUT. For that purpose, χ_{Tier3} was calculated according to (9) for the full range of exposure polarization states ($0^\circ \leq \tau \leq 180^\circ$ and $-45^\circ \leq \epsilon \leq 45^\circ$).

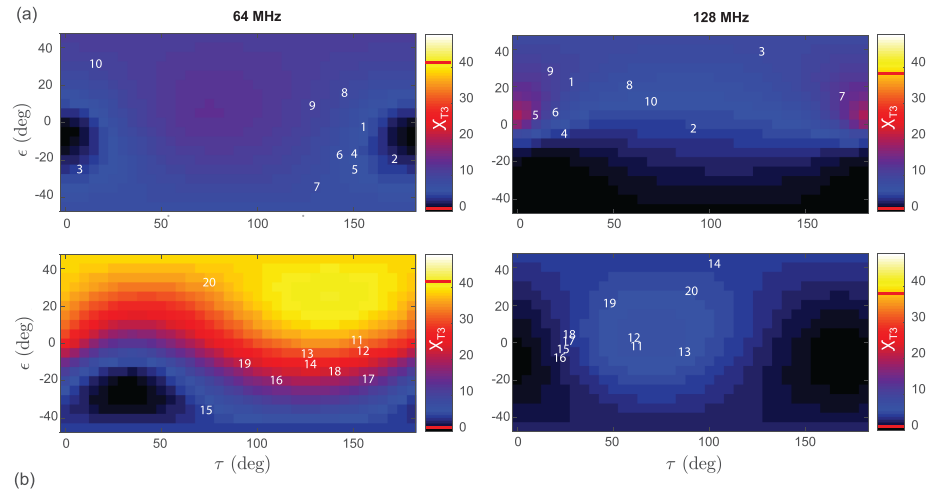


Figure 4. (a) Distributions of χ_{Tier3} in the (τ, ε) space at 64 MHz and 128 MHz, respectively, with the IUT placed along routing R1. χ_0 and χ_ϕ are highlighted with red solid lines on the colorbars. (b) Same as (a), but for IUT placement along routing R2. The white numbers inside the figures correspond to the numbering of the 20 selected exposure conditions along routing R1 (numbers 1–10) and routing R2 (numbers 11–20). The amplitude and phase variation of each exposure condition is shown in figure 5.

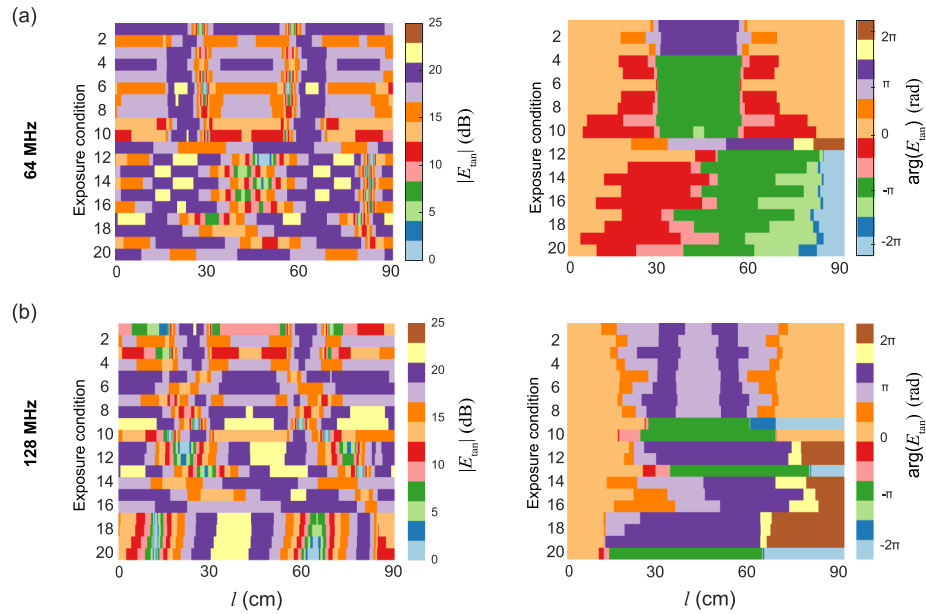


Figure 5. Characteristics of the complex-valued E_{tan} of the 20 selected exposure conditions identified for the TFD experiment. (a) Amplitude $|E_{\text{tan}}|$ (left) and phase $\arg(E_{\text{tan}})$ (right) of the $E_{\text{tan}}(l)$ along the implant routing trajectory l as a function of exposure condition at 64 MHz. (b) Same as (a), but for 128 MHz.

Figure 4 shows the distributions of $\chi_{\text{Tier3}}(\tau, \varepsilon)$ of the IUT at both 64 MHz and 128 MHz for the two selected routings, R1 and R2; χ_0 and χ_ϕ are highlighted with red solid lines on the colorbars. Diverse incident conditions to the IUT can be obtained by sampling χ_{Tier3} in the (τ, ε) space. The selected exposure conditions and associated χ_{Tier3} are marked in figure 4 for each frequency band and routing. Figure 5 shows the $E_{\text{tan}}(l)$ characteristics of the selected exposure conditions for both frequency bands. These selected exposures are then used for the radiated testing of the IUT.

The IUT is placed along the selected routings within the phantom of the experimental setup depicted in figure 2. The RF-coil is driven to achieve each of the polarization state of the B_1 field selected above (figure 4). During each exposure, the B_1 polarization state is reconstructed from the time-domain information recorded by the optical magnetic-field probes, and the magnitude of exposure is determined from the magnitude of E-fields at predefined locations recorded with the dosimetric probe EX3515 (SPEAG, Zurich, Switzerland), with a dynamic range of $10 \mu\text{Wg}^{-1}$ to 100mWg^{-1} and a sensor positioning uncertainty of ± 0.2 mm. The RF power deposition enhancement factor of the IUT, χ_{TFD} can then be easily obtained (Yao *et al* 2018).

Table 1. Comparison of power deposition (within the -30 dB iso-volume) obtained through Tier 3 (ISO 2018) predictions ($P_{\text{dep,Tier3}}$) and dosimetric validation measurements ($P_{\text{dep,TFD}}$). For more information about the comparison approach, e.g. regarding the handling of the background exposure that also exists in the absence of the implant (Yao et al 2018).

Exposure condition number	64MHz		128MHz	
	$P_{\text{dep,Tier3}}$ (mW)	$P_{\text{dep,TFD}}$ (mW)	$P_{\text{dep,Tier3}}$ (mW)	$P_{\text{dep,TFD}}$ (mW)
1	0.044	0.055	0.016	0.015
2	0.025	0.027	0.014	0.020
3	0.027	0.025	0.020	0.026
4	0.043	0.052	0.010	0.009
5	0.041	0.047	0.027	0.025
6	0.047	0.053	0.024	0.021
7	0.049	0.052	0.026	0.037
8	0.050	0.051	0.017	0.017
9	0.055	0.065	0.021	0.021
10	0.054	0.063	0.017	0.019
11	0.144	0.112	0.013	0.010
12	0.131	0.126	0.013	0.010
13	0.112	0.107	0.012	0.010
14	0.070	0.066	0.009	0.008
15	0.025	0.028	0.008	0.007
16	0.082	0.084	0.009	0.008
17	0.132	0.130	0.009	0.008
18	0.136	0.135	0.010	0.008
11	0.111	0.139	0.011	0.009
20	0.174	0.194	0.011	0.009

3. Results

The predicted power deposition values and those measured during the validation TFD experiments are compared in table 1 (at 64 MHz and 128 MHz). Figures 6 and 7 show the corresponding RF-heating enhancement factors of the IUT. The comparison of χ_{Tier3} calculated from (9), and the experimentally obtained χ_{TFD} is provided. The maximum deviations of χ_{TFD} from χ_{Tier3} are 1.0 dB and 1.5 dB for 64 MHz and 128 MHz exposure, respectively, which is within the estimated combined standard uncertainty of χ_{Tier3} and χ_{TFD} (table 2).

The effective B_1 polarization states during the exposure tests can slightly deviate from their theoretical target values and, therefore, each χ_{Tier3} shown in figures 6 and 7, is re-evaluated for the B_1 polarization state recorded during each exposure.

As shown in figures 6 and 7, test exposure configurations 1–10 show a different dynamic range of the enhancement factor χ than that of test configurations 11–20. This is due to the distinct routing selected for configurations 1–10 (R1) and 11–20 (R2). The observed RF-heating enhancement factor χ dynamic range of the IUT reaches from 0 to about χ_ϕ for 64 MHz exposure and up to $0.5\chi_\phi$ for 128 MHz. This is likely due to the roughly twofold higher transfer function phase range at 128 MHz, which increases the probability of destructive interference.

The uncertainty budget of the study comprises uncertainty factors associated with the TFD validation method and the transfer function approach. The TFD method uncertainty includes both experimental and numerical factors (table 2). The total combined uncertainties (obtained as the root-sum-square values of the various experimental and computational uncertainty contributions) of χ_{Tier3} and χ_{TFD} are found to be 1.36 dB and 1.5 dB, respectively (table 2). It should be noted that, for a comprehensive uncertainty budget analysis of *in vivo* Tier 3 power deposition, the uncertainty related to the *in vivo* incident evaluation (e.g. the anatomical routing, anatomical modelling, tissue variety, etc) should also be included.

4. Discussion

In this paper, a new method that reduces the required number of different routings and improves the exposure fidelity for a comprehensive transfer function validation of AIMDs with elongated leads has been proposed. With the proposed TFD test setup, each routing provides sets of diverse distinguished exposure conditions through changing the polarization of \vec{B}_1 .

The diversity of the exposure conditions was maximized by selecting polarization states that exploit the full achievable enhancement factor χ range. Further diversification could be achieved by introducing other

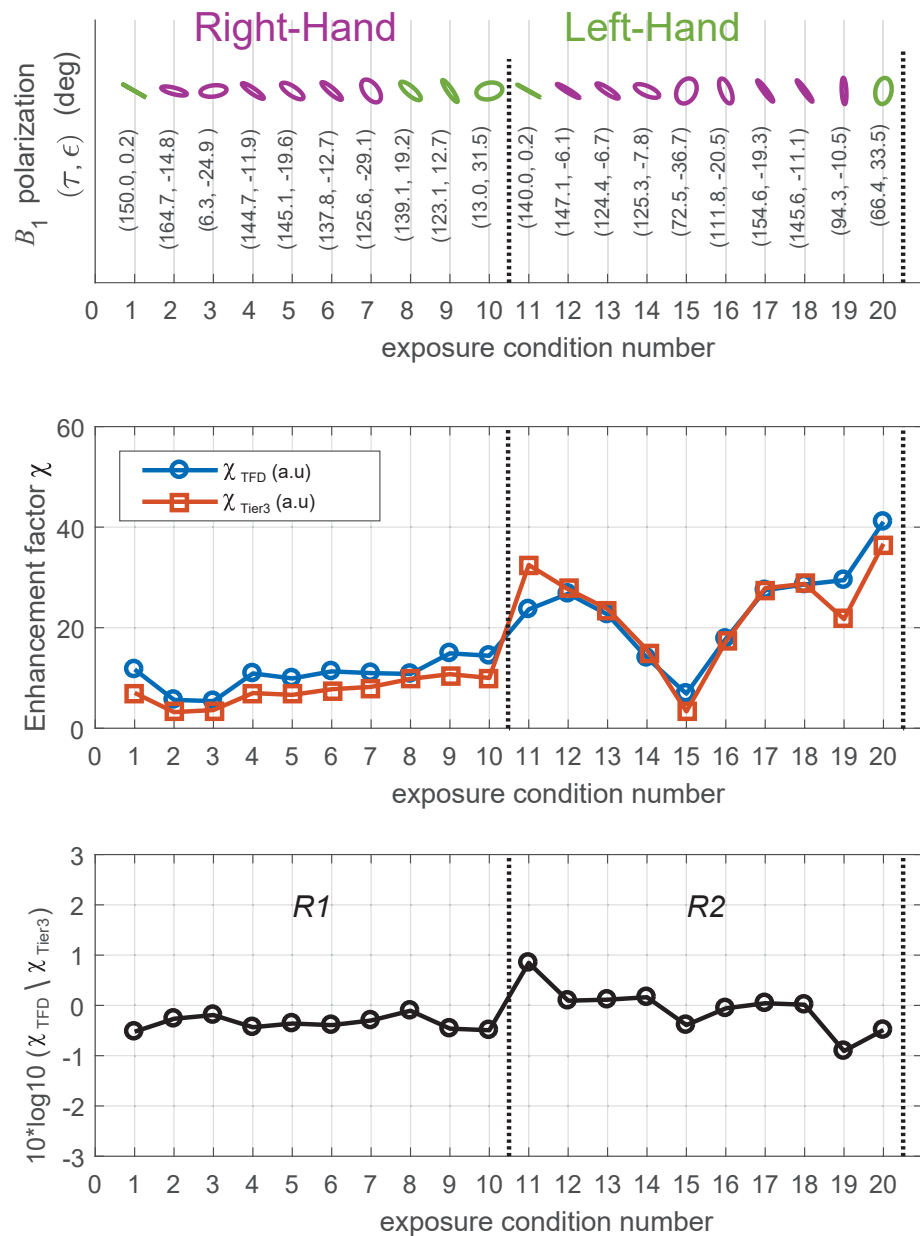


Figure 6. Summary of the TFD experiment on RF-induced heating enhancement, evaluated for the IUT at 64 MHz. Twenty exposure test configurations were selected to sample the dynamic range of IUT RF-induced heating enhancement. Top: B_1 polarization states of the selected exposure test configurations. The left-hand and right-hand polarized exposures are indicated in green and purple, respectively. Middle: Measured and calculated RF-heating enhancement factors, χ_{TFD} and χ_{Tier3} , of the selected exposure test configurations. Bottom: Deviation between measured χ_{TFD} and Tier 3 (ISO 2018) calculated χ_{Tier3} .

unique test routings or by increasing the number of the birdcage coil channels. At this point, it is useful to present a mathematical framework that could be employed to systematically select exposure conditions that maximize sensitivity and validation information content, potentially allowing further reduction of the required number of test conditions.

\vec{E}_{tan} exposures for different (channel-)driving vectors $\{v\}$ are simply linear combinations of the \vec{E}_{tan} exposures of the N individual channels ($\vec{E}_{\text{tan},i}$ where $N = 2$ and $i = x, y$ in our experimental setup). As such, there are at maximum N truly independent exposure conditions, and it can at first appear counter-intuitive that there is additional value in testing further linear combinations. However, the transfer functions are defined over a continuous, non-discrete length interval, and so are possible deviations from the true transfer functions. Therefore, the transfer function error-space in infinitely-dimensional and different deviation functions show different sensitivity to exposure conditions (see below for a mathematical quantification thereof). It follows that the different excitation conditions applied by the TFD method still provide additional validity information. This can readily be understood when variational calculus is applied to

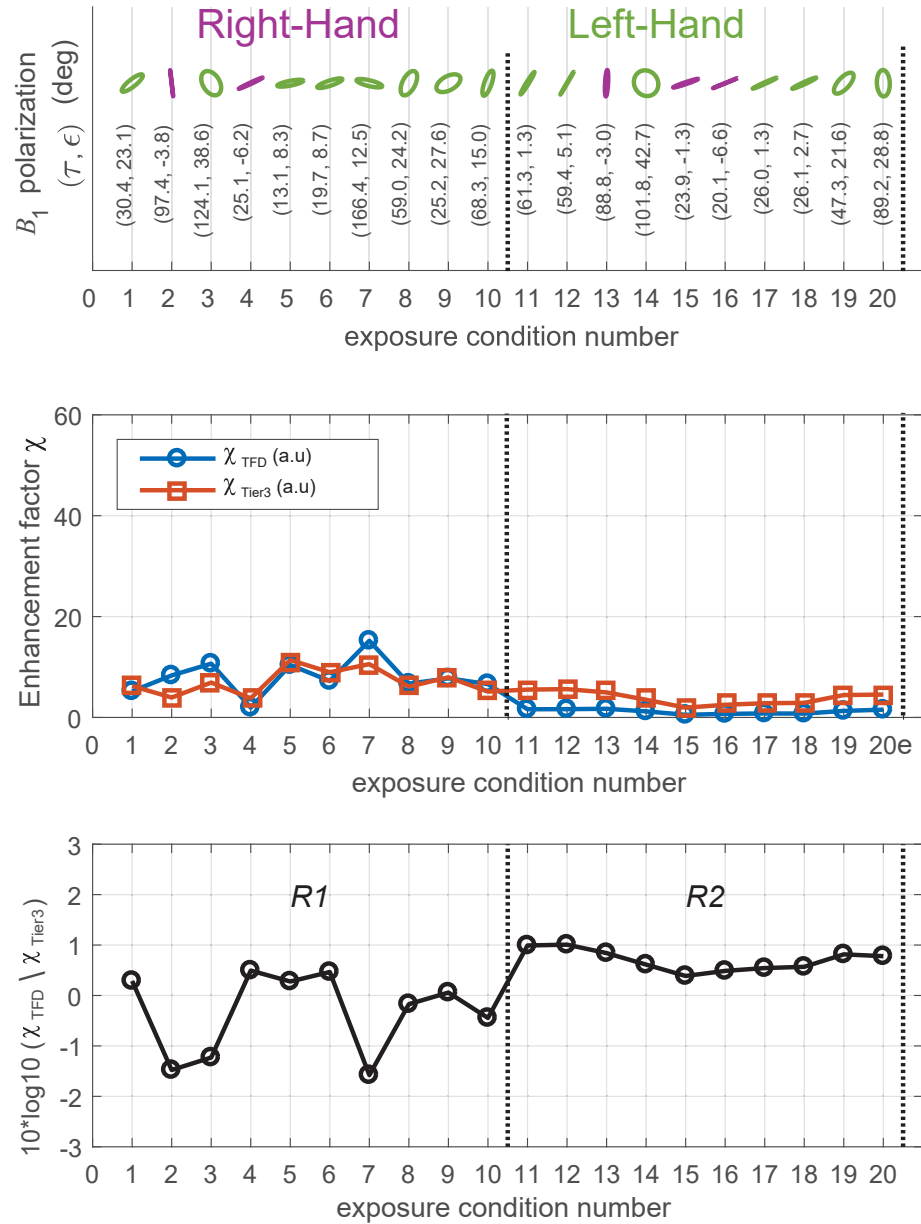


Figure 7. Summary of the TFD experiment on RF-induced heating enhancement, evaluated for the IUT at 128 MHz. Twenty exposure test configurations were selected to sample the dynamic range of IUT RF-induced heating enhancement. Top: B_1 polarization states of the selected exposure test configurations. The left-hand and right-hand polarized exposures are indicated in green and purple, respectively. Middle: Measured and calculated RF-heating enhancement factors, χ_{TFD} and χ_{Tier3} , of the selected exposure test configurations. Bottom: Deviation between measured χ_{TFD} and Tier 3 (ISO 2018) calculated χ_{Tier3} .

determine the impact of errors in the amplitude $A(l)$ or phase $\phi(l)$ of the transfer function $h(l) = A(l)e^{i\phi(l)}$ on the enhancement factor χ defined in (8):

$$\frac{\delta\chi}{\delta A(l)} = 2\text{Re} \left[E_{\text{tan}}(l) e^{i\phi(l)} F_{\text{norm}}^* \right] \quad (10)$$

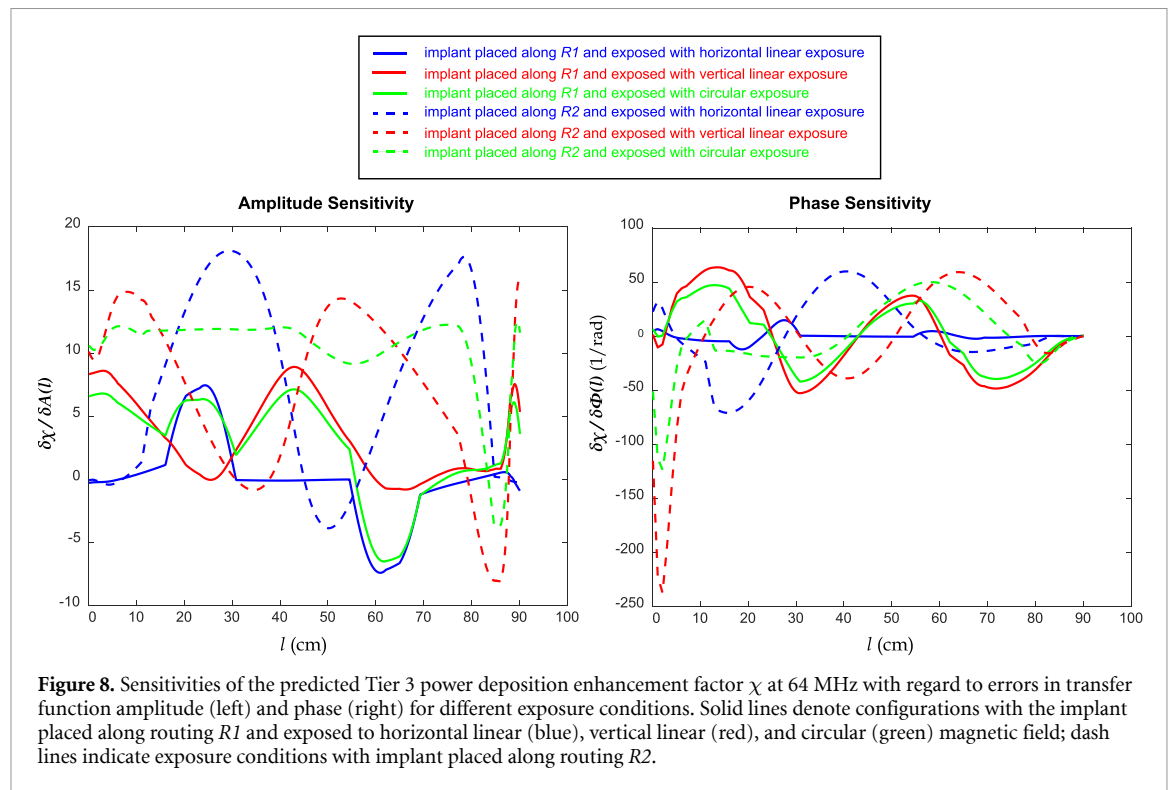
$$\frac{\delta\chi}{\delta\phi(l)} = -2\text{Im} \left[E_{\text{tan}}(l) A(l) e^{i\phi(l)} F_{\text{norm}}^* \right] \quad (11)$$

where $\frac{\delta\chi}{\delta A(l)}$ and $\frac{\delta\chi}{\delta\phi(l)}$ represent the sensitivities (functional derivatives) of the enhancement factor χ of the IUT Tier 3 power deposition with respect to transfer function amplitude errors $\delta A(l)$ and phase errors $\delta\phi(l)$, respectively. $\text{Re}[\]$ and $\text{Im}[\]$ indicate the real and imaginary parts, and

$$F_{\text{norm}} = \frac{1}{|E_0|^2} \int_0^L \vec{E}_{\text{tan}}(l') A(l') e^{i\phi(l')} dl'. \quad (12)$$

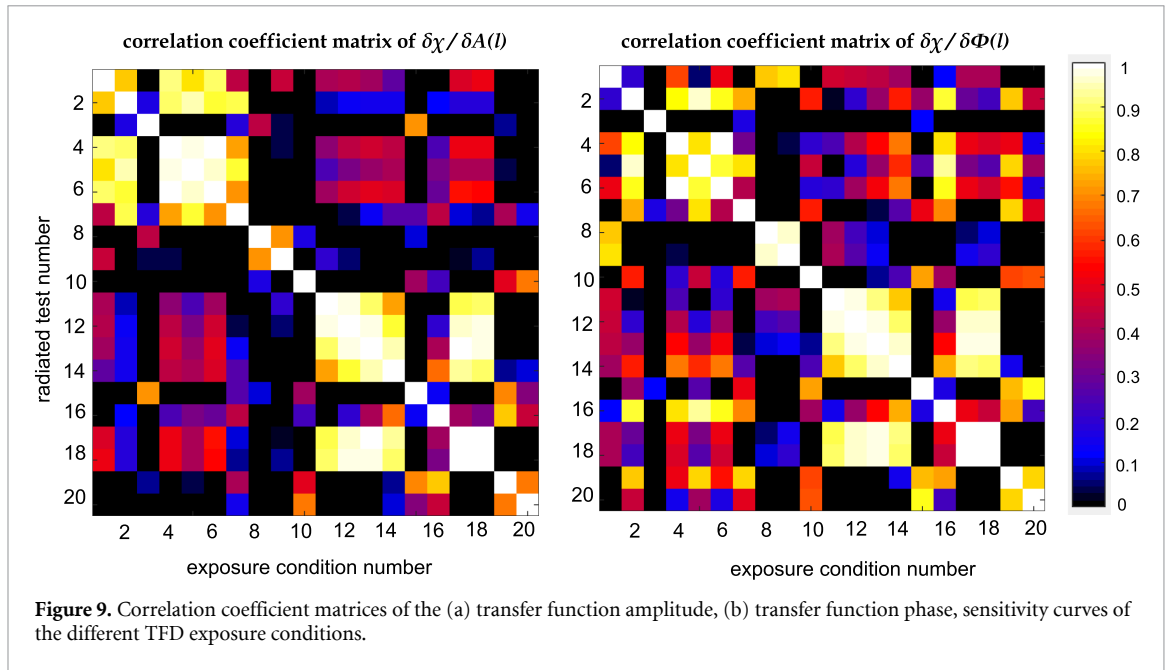
Table 2. Uncertainty budget of enhancement factor χ evaluation

Source	χ_{Tier3} Uncertainty (dB)	χ_{TFD} Uncertainty (dB)
TFD exposure		
experimental setup	-	0.86
numerical modeling	0.68	0.68
Local enhancement evaluation		
data acquisition system	-	0.52
TSM	-	0.25
post-processing (Yao <i>et al</i> 2018)		0.88
Tier 3 model (Park <i>et al</i> 2007)		
piecewise excitation system (Zastrow <i>et al</i> 2016)	1.18	-
Combined Uncertainty ($k = 1$)	1.36	1.50



It is apparent from (10) and (11) that χ is sensitive to errors at locations where $E_{\text{tan}}(l)$ (resp. $E_{\text{tan}}(l) \cdot A(l)$) is large. Therefore, linear combinations of the different channels, which—thanks to complex interference—maximize exposure at locations of interest along the lead, can result in measurement configurations that are particularly sensitive to errors in $h(l)$ at these locations (provided $|h(l)|$ is not too small at these locations, which would again reduce sensitivity). Figure 8 shows the sensitivities of the predicted enhancement factor χ of the IUT Tier 3 power deposition with regard to transfer function amplitude and phase errors for different \vec{v} (linear and circular polarization (CP) modes). It can be seen how the two different channels have vastly different sensitivities, and how the combined CP mode is also sensitive to localized errors. A more comprehensive picture can be seen in figure 9, where the correlation coefficient matrices of the sensitivity curves of the different TFD exposure conditions are shown (amplitude and phase error sensitivity). While some strong off-diagonal correlations indicate that, e.g. exposure conditions 2 and 4–6 are not optimally orthogonal, the diagonal is dominant and only 22 % (31 %) of the off-diagonal coefficients are larger than 0.5 for the amplitude (phase) sensitivities.

To demonstrate how different χ measurements can be used with varying \vec{v}^j (the j th exposure configuration) to constrain the error of $h(l)$, the suitability of such measurements for the reconstruction of $h(l)$ are investigated independently from the $h(l)$ measurement approach by piecewise excitation. For that purpose, we assume that $A(l)$ and $\phi(l)$ can be approximated by finite numbers (n_A and n_ϕ) of the cosine



expansion terms (see appendix): $\tilde{A}(l; \vec{c}_A) = \sum_{p=0}^{n_A-1} c_{A,p} \cos(2\pi p \frac{l}{L})$ and $\tilde{\phi}(l; \vec{c}_\phi) = \sum_{q=0}^{n_\phi-1} c_{\phi,q} \cos(2\pi q \frac{l}{L})$. Then, we can define the residual function:

$$f_{\text{res}}(\vec{c}_A, \vec{c}_\phi) = \sum_t \sum_j \left(\frac{1}{|E_0|^2} \left| \int_0^L \vec{E}_{\text{tan},t}^j(l) \tilde{A}(l; \vec{c}_A) e^{i\tilde{\phi}(l; \vec{c}_\phi)} \cdot d\vec{l} \right|^2 - \chi_{\text{meas},t}^j \right)^2 \quad (13)$$

where $\vec{E}_{\text{tan},t}^j = \sum_{i=1}^N \{v^j\}_i \vec{E}_{\text{tan},i,t}$ is the tangential incident field strength along trajectory t , for the coil driving vector $\{v^j\}$. Subsequently f_{res} can be minimized with the *fminsearch* function in Matlab (The MathWorks, Inc. Natick, Massachusetts, USA). To provide comparable weight to the different excitations $\{v^j\}$, the field intensities have been scaled such that $|\vec{E}_{\text{tan}}| = 1 \text{ Vm}^{-1}$. Values on the order of 10 are found to be suitable (a balance between accuracy and convergence) for both n_A and n_ϕ .

Figure 10 illustrates how well $h(l)$ (phase and amplitude) can be reconstructed by minimizing $f_{\text{res}}(\vec{c}_A, \vec{c}_\phi)$. Three reconstructions are compared: i) with the measurement data from routing $R1$ only, ii) with only the data from routing $R2$, and iii) with both. The reconstruction quality is comparable to how well $h(l)$ can be approximated by its cosine transformation (see appendix: Suitability of cosine expansion) and also depends on the precision of E_{tan} . Figure 11 shows how well the different approaches fit the measured χ values (in comparison also to those evaluated with the measured $h(l)$). As expected, the exposure configurations that were used to reconstruct $h(l)$ fit the results best. To ensure independent validation, it is important that the transfer function is determined in a system completely different than the validation system, e.g. by means of the piecewise excitation technique (Zastrow et al 2016) that employs a different phantom and very different exposures, i.e. to a dipole antenna.

The finding that the transfer functions reconstructed from the measured TFD enhancement factors closely resemble the experimentally measured transfer function demonstrates that i) the TFD exposure conditions are indeed sufficiently orthogonal to constrain the band of possible transfer function errors and ii) the TFD approach is suitable for transfer function validation.

A further increase in validation power (and a reduction of the associated $h(l)$ uncertainty) could be achieved by optimizing $\{v^j\}$ such that i) sensitivity to errors in $A(l)$ and $\phi(l)$ is maximized, along with ii) the additional independent information provided by each individual $\{v^j\}$ (minimization of $E_{\text{tan},t,j}$ correlations). This can be done based on (10) and (11).

The methodologies introduced in this study (maximization of E_{tan} diversity by full sampling of the enhancement factor variability range) can be used to optimize the validation power of the TFD method and to reduce the associated uncertainty on an individual implant basis. In view of the similarity of many transfer functions for certain device classes and frequency bands, it is also possible to prescribe corresponding, carefully chosen, fixed and generally applicable exposure conditions for routine evaluations. One limitation of the TFD method is its sensitivity to misplacement of the transverse plane normal to the z axis of the birdcage test coil, where the implant lies, because of the strong dominance of the electric field component in

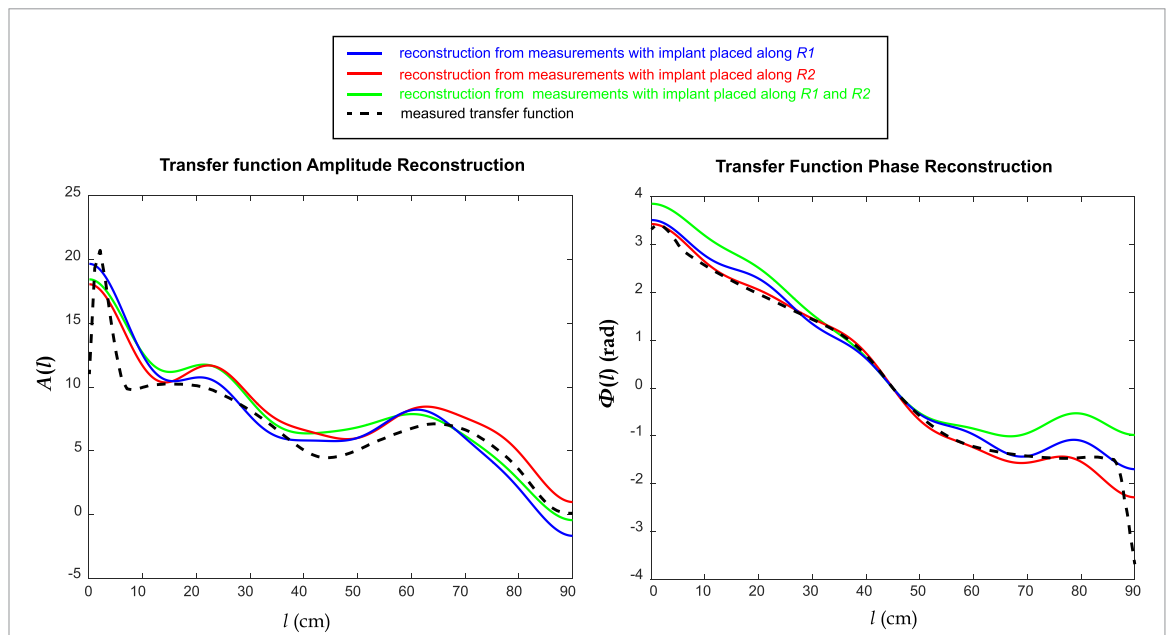


Figure 10. Amplitude (left) and phase (right) reconstruction of the IUT RF transfer function at 64 MHz based on the measurement data from routing $R1$ only (blue), routing $R2$ only (red), and both $R1$ and $R2$ (green) to minimize the residual function f_{res} in (13). The RF transfer function measured by the piecewise excitation technique is also shown (dashed line).

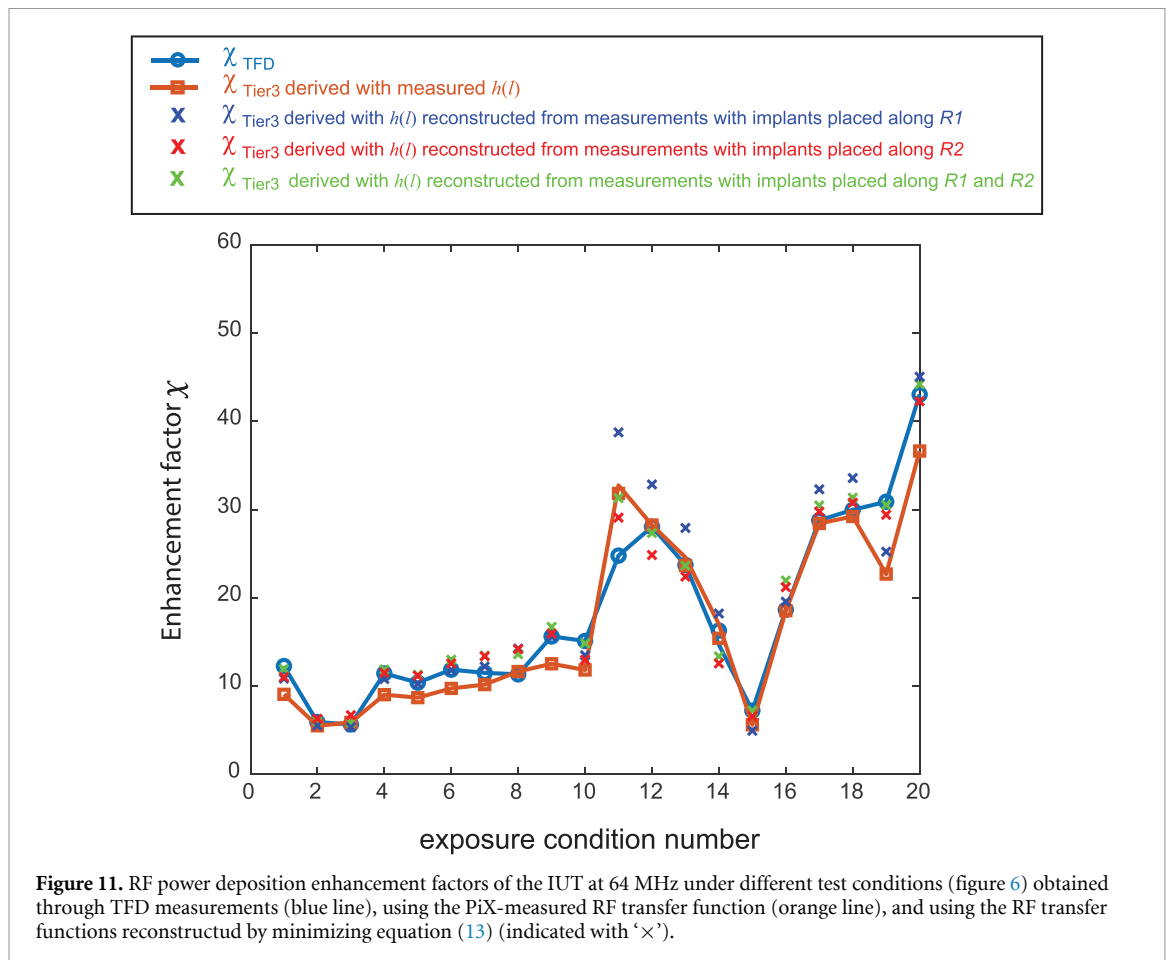


Figure 11. RF power deposition enhancement factors of the IUT at 64 MHz under different test conditions (figure 6) obtained through TFD measurements (blue line), using the PiX-measured RF transfer function (orange line), and using the RF transfer functions reconstructed by minimizing equation (13) (indicated with 'x').

this axis. Nevertheless, the main strength of the TFD method is its speed: For the same number of validation test configurations (20 in this case), the time required by TFD is about 20 times less than that for the methods applied in the literature (ISO 2018, Calcagnini et al 2008, Mattei et al 2008, Mattei et al 2015, Neufeld et al 2009, Nordbeck et al 2009, Zastrow et al 2011).

While the TFD method has been developed and optimized for the described exposure system, it is also applicable to other test systems (e.g. different RF coil geometries, tissue simulating media, etc). However, its performance and associated uncertainties would have to be re-investigated for each implementation. The next step is to extend the methodology to ultra-high fields that requires development of the corresponding equipment and reassessment of all the sensitivities.

5. Conclusions

Based on the finding that the amplitude and phase of the incident tangential electrical field along a single lead path in a cylindrical phantom can be sufficiently varied by changing the polarization of the incident magnetic field inside standard birdcage RF coils, a TFD method is proposed in this work to provide diverse incident conditions to the IUT while preserving the fidelity of the incident conditions, which allows efficient and reliable characterization of transfer function of AIMD with elongated leads.

The proposed AIMD exposure setup has been characterized and validated and meets the requirements regarding negligible backscattering effects between AIMD sections and phantom boundaries. The uncertainty ($k = 1$) of the incident conditions associated with the phantom and provided IUT is 0.86 dB (table 2).

The TFD method was successfully applied to a 90 cm long IUT, and the deviation of the experimentally evaluated RF-heating from theoretical values is less than the combined standard uncertainty of 2 dB (root-sum-square of 1.36 and 1.5 dB in table 2). Therefore, the TFD method offers validation of the RF transfer function of implanted leads in MRI reliably and within a fraction of time compared to other methods.

Acknowledgments

The authors would like to thank Sabine Regel of SR Scientific GmbH, Arya Fallahi, and Patricia L Bounds for the careful review of the manuscript.

Declaration of conflict of interest

None

Appendix: Suitability of cosine expansion

The approximation of the phase and amplitude of $h(l)$ for an AIMD without lumped elements by a cosine expansion is motivated by the following factors: i) appreciation of the curve shape (continuous, without sharp bends but oscillating); ii) a desire to avoid complex-valued decompositions (such as the Fourier transformation), because of the real-valued nature of A and ϕ and because performing a complex derivative to evaluate (10) and (11) is not possible (violation of the Cauchy-Riemann equations); iii) the recognition that numerical investigations have shown that the cosine approximation can approximate $h(l)$ well, with a moderate number of terms.

However, it should be noted that the cosine transformation assumes a symmetric function, which enforces a zero derivative at $l = 0$ that is not present in $h(l)$ —in fact $h'(0)$ is relatively steep. Therefore, the fit cannot be expected to be perfect in that region. Investigations involving seven experimentally determined AIMD transfer functions have shown that the cosine transformation provides superior results in comparison with the sine function and is always able to approximate $h(l)$ with a small standard deviation.

With regard to the mathematical analysis in section 4, it should be pointed out that using the cosine expansion with a limited number of terms is a way of reducing the infinitely-dimensional space of possible transfer function errors to a finite dimension. It is only permissible due to the observed continuous and smooth nature of the measured or computed transfer functions.

ORCID iD

Theodoros Samaras  <https://orcid.org/0000-0003-0170-4520>

References

- Brink W M, Gulani V and Webb A G 2015 Clinical applications of dual-channel transmit MRI: A review *J. Magn. Reson. Imaging* **42** 855–69

- Brink W M, Remis R F and Webb A G 2016 A theoretical approach based on electromagnetic scattering for analysing dielectric shimming in high-field MRI *Magn. Reson. Med.* **75** 2185–94
- Cabot E, Lloyd T, Christ A, Kainz W, Douglas M, Stenzel G, Wedan S and Kuster N 2013 Evaluation of the RF heating of a generic deep brain stimulator exposed in 1.5 T magnetic resonance scanner *Bioelectromagnetics* **34** 0197–8462
- Calcagnini G, Triventi M, Censi F, Mattei E, Bartolini P, Kainz W and Bassen H I 2008 In vitro investigation of pacemaker lead heating induced by magnetic resonance imaging: Role of implant geometry *J. Magn. Reson. Imaging* **4** 879–86
- de Heer P, Brink W M, Kooij B J and Webb A G 2012 Increasing signal homogeneity and image quality in abdominal imaging at 3 T with very high permittivity materials *Magn. Reson. Med.* **68** 1317–24
- ISO 10974:2018 2018 Assessment of the safety of magnetic resonance imaging for patients with an active implantable medical device *Technical Report* (Int. Organization for Standardization) Geneva, Switzerland
- Kraus J D and Carver K R 1973 *Electromagnetics* (New York: McGraw-Hill Education)
- Mattei E, Gentili G, Censi F, Triventi M and Calcagnini G 2015 Impact of capped and uncapped abandoned leads on the heating of an MR-conditional pacemaker implant *Magn. Reson. Med.* **73** 390–400
- Mattei E, Triventi M, Calcagnini G, Censi F, Kainz W, Mendoza G, Bassen H I and Bartolini P 2008 Complexity of MRI induced heating on metallic leads: Experimental measurements of 374 configurations *Biomed. Eng. Online* **7** 11
- Neufeld E, Kuehn S, Szekely G and Kuster N 2009 Measurement, simulation, and uncertainty assessment of implant heating during MRI *Phys. Med. Biol.* **54** 4151–69
- Nordbeck P et al 2009 Measuring RF-induced currents inside implants: Impact of device configuration on MRI safety of cardiac pacemaker leads *Magn. Reson. Med.* **61** 570–8
- Park S M, Kamondetdacha R and Nyenhuis J A 2007 Calculation of MRI-induced heating of an implanted medical lead wire with an electric field transfer function *J. Magn. Reson. Imaging* **26** 1278–85
- Pokovic K, Schmid T, Frohlich J and Kuster N 2000 Novel probes and evaluation procedures to assess field magnitude and polarization *IEEE Trans. Electromag. Compat.* **42** 240–4
- Yao A, Zastrow E and Kuster N 2018 Data-driven experimental evaluation method for the safety assessment of implants with respect to RF-induced heating during MRI *Radio Sci.* **53** 700–9
- Zastrow E, Cabot E, Christ A and Kuster N 2011 Experimental phantoms for the assessment of medical implant leads induced SAR under a linear-phase incident field condition *XXXth URSI General Assembly and Symp.*
- Zastrow E, Capstick M and Kuster N 2016 Experimental systems for RF-heating characterization of medical implants during MRI *ISMRM 2016 24th Ann. Meeting and Exhibition (Singapore, 7–13 May 2016)* (available at: <https://index.miramart.com/ISMRM2016/PDFfiles/0912.html>)
- Zastrow E, Yao A and Kuster N 2017 Practical considerations in experimental evaluations of RF-induced heating of leaded implants *XXXIInd URSI General Assembly and Symp. (Montreal, QC, 19–26 August 2017)* (available at: <https://doi.org/10.23919/URSIGASS.2017.8105350>)